Micromechanical resonant cantilever sensors actuated by fringing electrostatic fields

OPEN ACCESS
IOP Publishing
Journal of Micromechanics and Microengineering
J. Micromech. Microeng. **32** (2022) 054001 (12pp)
https://doi.org/10.1088/1361-6439/ac5a61

Micromechanical resonant cantilever sensors actuated by fringing electrostatic fields

Naftaly Krakover[1,2,*], **B Robert Ilic**[3] **and Slava Krylov**[1]

[1] Faculty of Engineering, School of Mechanical Engineering, Tel Aviv University, Ramat Aviv, Tel Aviv 69978, Israel
[2] MANOR A.D.T. Division, Rafael Advanced Defense Systems Ltd, Haifa 31021, Israel
[3] Center for Nanoscale Science and Technology, National Institute of Standards and Technology, Gaithersburg, MD 20899, United States of America

E-mail: naftalykrakover@gmail.com

Received 13 October 2021, revised 7 February 2022
Accepted for publication 3 March 2022
Published 17 March 2022

Abstract

We report on the architecture and operational principle of a resonant cantilever-type displacement sensor. The device is actuated electrostatically by a side electrode that is coplanar with the cantilever and by a gap-closing electrode positioned underneath the beam. The unique electrode geometry combined with the appropriate actuating voltages allows positioning of the cantilever in close proximity to the bistability threshold, where the frequency sensitivity to the electrode displacement is enhanced. Using a reduced order model backed by numerical simulations, the dependencies of the device frequency on the beam's deflections and the actuation voltages were mapped. We show wide-range tunability that spans a range between softening and hardening behavior. We demonstrate displacement sensing using fabricated single crystal silicon ≈2000 μm long, ≈5 μm thick cantilevers. When compared to a resonant cantilever sensor actuated solely by a gap-closing electrode, measurements from our fringing field actuated devices show a four times higher sensitivity of ≈98 Hz μm^{-1}. The suggested approach may find applications in a broad range of micro and potentially nano-scale applications including resonant inertial, force, mass and bio-sensors.

Keywords: resonant cantilever sensor, electrostatic actuation, fringing field, bistability, MEMS

(Some figures may appear in colour only in the online journal)

1. Introduction

Resonant micro- and nano-scale cantilevers are among the most established sensing elements implemented in the fields of engineering, life and physical sciences [1, 2]. These devices were shown to be indispensable for the detection of extremely small masses [3], biomolecular binding events [4], and for non-contact topographic and localized charge imaging using atomic force microscopy (AFM) [5]. The key advantages of cantilevers (when compared to doubly clamped beams of comparable dimensions) are their lower stiffness, better linearity and reduced sensitivity to temperature and residual stress. In resonant cantilever-type devices, the sensing paradigm is commonly based on measuring the beam's spectral characteristics that are affected by structural variations in the stiffness or the mass. Following the emergence of cantilever sensors, significant progress has been achieved in the design and operational protocols of the devices by confining the vibrations within the linear resonance regime. A possibility to explore nonlinearity

* Author to whom any correspondence should be addressed.

as a tool for the performance enhancement in resonant sensors has attracted significant attention within the research community [6, 7]. In contrast to the linear resonators whose natural frequencies are independent on the applied forces and vibrational amplitudes, in nonlinear systems the spectral characteristics of the device are affected by the configuration-dependent forces, which are directly related to the resonant frequency of the device [5].

In electrostatically actuated microelectromechanical systems (MEMS)—based devices, both structural geometric nonlinearity (as in double-clamped initially curved bistable beams [7]) and nonlinearity of the actuating forces are present. In devices actuated by parallel-plate (PP), gap-closing electrodes, the intrinsic dependence of the electrostatic loading on the system configuration manifests itself in the decrease of the device stiffness and frequency with increase of the actuation voltage. This electrostatic softening is a beneficial feature allowing for voltage-based frequency tuning. The method is widely used in applications as a tool to compensate for fabrication-related uncertainties in the device geometry and in the operational conditions [7, 8]. One of the distinguishing features of electrostatically actuated devices is that they can be prone to the so-called pull-in (PI) instability. Within this regime, the structure collapses toward the electrode at actuating voltages above a certain critical value [9, 10]. While often viewed as a drawback, PI lies at the foundations of several strategies for sensitivity enhancement. Specifically, when the structure is found in a configuration close to the instability threshold, even a minute change in the loading or environmental parameters may result in a stability loss and thus in a major change in the device response. Enhanced sensitivity in the vicinity of the PI was exploited in the event-based (binary, bifurcation-based) sensors [11–14] where the collapse of the device toward the actuating electrode was initiated by an added mass or acceleration [14, 15]. In resonant sensors, when the device is driven near the critical configuration, the effective stiffness and therefore the natural frequency both approach zero in such a manner, that significantly enhances frequency sensitivity to the loading or deflection [16–21].

However, operation near the instability limit has its own drawbacks. Since the PI collapse of the device toward the electrode initiates contact between the two surfaces, the impact interaction may result in irreversible damage affecting the long-term repeatability of the sensor scale factor. For this reason, most of the sensors based on this scenario are driven far enough from the PI point, at the expense of inferior performance. To benefit from the increased sensitivity in the vicinity of the critical configurations while avoiding the associated risks, alternative operational scenarios were suggested. For example, in bistable curved micromechanical beams [14, 22] or offset double-clamped beams [18, 19, 23, 24] stability loss event is not accompanied by contact, which allows reversible operation. (Hereafter, bistability is defined as an ability of the device to stay in two different equilibrium configurations at the same loading/voltage, whereas the term 'latching' property is reserved for a particular case when the structure is able to remain in a stable buckling state at zero voltage.) Resonant sensing near the bistability threshold of lithographically defined, curved double-clamped $\approx$1000 μm long and $\approx$3 μm wide micromechanical Si beams actuated by a movable PP electrode was reported in [22], where the sensitivity up to $\approx$1.5 Hz nm^{-1} was experimentally demonstrated.

The main limitation of the statically indeterminate double-clamped beams is that they are sensitive to temperature and residual stress [25, 26]. Namely, the temperature variations in the fully constrained double-clamped beams inevitably give rise to thermal stresses. While residual stress is generally affected by several factors such as fabrication processing or packaging design, in many cases it is related to the thermal stress. Cantilever-based devices (made of one material and not from a multilayer stack), which are statically determinate and may extend or contact freely with varying temperature, are distinguished by an intrinsically lower sensitivity to temperature and residual stress. This motivates the wide use of these structures in sensing applications. (Of course, stress gradients, especially in the regions close to the cantilever clamping point and originated in thermal mismatch between the materials of the package stack, may result in certain bending of the beams. Since the main goal of the present work was to investigate the sensing principle based on high frequency tunability of our device, the packaging and integration issues were out of the scope of the study.) However, cantilevers are mechanically linear and cannot be bistable, which prevents the realization of the advantages gained from the operation near the critical configurations. Here we investigate a cantilever-based architecture that allows frequency sensitivity enhancement which is typically encountered in nearly bistable devices. The approach is based on the implementing of a tailored electrode geometry and fringing electrostatic field actuation. In turn, this architecture introduces a nonlinearity required to achieve bistable or nearly bistable behavior. By appropriately tuning the actuation voltages, the cantilever can be positioned in a configuration at the bistability threshold where the frequency sensitivity enhancement occurs.

Fringing field electrostatic actuation was previously shown to be useful for different purposes [27–30]. Efficient parametric excitation and frequency tuning in fringing-field actuated micromechanical beams were explored in [20, 31–34]. Repulsive fringing-field electrostatic forces were implemented for energy harvesting [35], and for operation of microswitches [36], micromirrors [37, 38], and microphones [39]. Fringing field actuation of a resonant device by means of a dielectric Kelvin polarization force was demonstrated in [30]. In all these works, a possibility of the sensitivity enhancement through operation near stability boundaries was not mentioned or discussed.

The concept of a bistable cantilever presented here was first introduced in [40]. It was shown, using the model, that combination of the fringing electrostatic field actuation with loading by a PP electrode may result in bistability of the device and in a wide-range tunability of its fundamental frequency. Experimental demonstration of the displacement sensing using fringing-field cantilever was reported in [41]. While the functionality of the device used as a pressure sensor was illustrated in this work, the sensitivity enhancement effect was not demonstrated. Efficient electrostatic up-tuning of the

beam's frequency and enhancement of the device frequency to voltage sensitivity in the fringing-field actuated cantilever was recently reported in [42]. However, fabrication process of the device implementing an alternative architecture of the electrodes, which are thicker than the cantilever itself, required multilevel critically timed etching steps. The added complexity from the multi-step timed etch are less controllable when compared to the device within the present work.

Here we investigate, both theoretically and experimentally, the feasibility of the suggested sensitivity improvement approach in a fringing field actuated cantilever-type device. In contrast to our previous works [40, 41], a detailed analysis of the device's dynamics is presented. We show the mapping of the design and operational parameters, the experimental demonstration of both stiffening and softening behavior, and enhanced sensitivity.

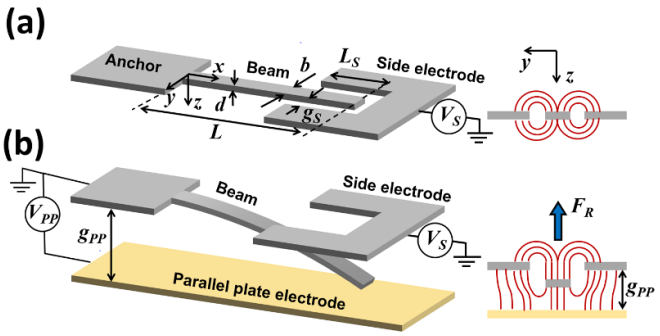

Figure 1. (a) Schematics of an undeformed cantilever actuated by symmetric fringing fields emerging from the side (fringing) electrode. (b) Deformed beam simultaneously actuated by a parallel-plate (PP) and side (S) electrodes connected to the voltages V_{PP} and V_{S}, respectively. Insets illustrate schematics of the fringing fields for each case. Large arrow shows the restoring force F_{R}.

2. Model and operational principle

A prismatic cantilever of a length L, width b and thickness d is assumed to be made from a linearly elastic material (silicon) with the Young's modulus E (in the x-direction) and density ρ, figure 1(a). A planar side (S) electrode of length L_{S} surrounding the beam is located at a distance g_{S} from the beam and has the same thickness d as the beam. The cantilever can freely deflect in the out-of-plane (z) direction whereas its in-plane (y) deflection is precluded due to the high width to the thickness ratio (b/d). A PP electrode is located under the beam, at the distance (the gap) g_{pp}, figure 1(b). The beam is grounded, while the voltages V_{s} and V_{pp} are applied to the S and the PP electrodes, respectively.

To highlight ideas beyond the sensitivity enhancement paradigm investigated in this work, we first describe qualitatively the device behavior and the role for each of the actuating forces acting on the beam. The deformed cantilever, figure 1(b), is actuated by the electrostatic forces of two types. The first is associated with the fringing fields emerging from the S electrode. Since the fringing field actuation force generally cannot be described analytically in a closed form, it is convenient to approximate this force by the following expression [31]

$$f_{\mathrm{s}}(x,t) = -\frac{\alpha\sigma\,(w/d)\,V_{\mathrm{s}}^2}{1+\sigma|w/d|^p} \qquad (L_{\mathrm{S}} \le x \le L)\,. \tag{1}$$

Here $f_{\mathrm{s}}(x,t)$ is the force per unit length of the cantilever, $w = w(x,t)$ is the beam's deflection (positive in the positive z-direction), V_{S} is the voltage applied to the S electrode and α, σ, p are the geometry-dependent fitting parameters. The approximation (1) was previously shown to represent the fringing field electrostatic force with good accuracy [31].

The second actuating force is the electrostatic force provided by the PP electrode. It is approximated by a simple PP capacitor formula

$$f_{\mathrm{PP}}(x,t) = \frac{\varepsilon_0 b V_{\mathrm{PP}}^2}{2(g_{\mathrm{PP}}-w)^2} \tag{2}$$

where $\varepsilon_0 = 8.854\times10^{-12}$ F m^{-1} is the dielectric permittivity of vacuum.

The electrostatic actuation forces f_{s} and f_{PP} are shown schematically on figure 2(a) along with the linear elastic restoring force. Due to the symmetry of the electrostatic field, the force provided by the S electrode is zero when the beam is in the initial, undeformed configuration. In the deflected state, as a result of the fringing fields asymmetry, f_{s} acts in the direction opposite to the beam's deflection and effectively serves as a restoring force [31]. In contrast, f_{PP} is divergent and pulls the beam toward the electrode and further away from its initial configuration. Moreover, this force grows infinitely when the beam approaches the electrode, which may result in the PI instability [43]. Equilibrium curves corresponding to the actuation solely by the PP electrode and by the combination of both PP and the S electrodes are shown schematically in figure 2(b). The frequencies of the linear, small-amplitude, free vibrations around the equilibria are shown on figure 2(c). In the case when the beam is actuated solely by the PP electrode, the equilibrium curve is typical for a spring-capacitor model and contains only one limit point (the point of maximum) associated with the PI instability. When the S electrode force is added, an inflection point emerges within the equilibrium curve. Since the slope at the inflection point decreases with increasing V_{S}, the effective stiffness and therefore the frequency of the beam at this point can be tailored to an arbitrarily low value [40]. For V_{S} higher than a certain critical value, two additional points of extremum—the local maximum (snap-through ST) and minimum (release R) appear at the equilibrium curve indicating that the system is bistable [40]. As suggested by figure 2(c), near the critical (ST, R and PI) limit points the slope of the frequency–deflection curve approaches zero and therefore the sensitivity of the frequency to deflection is pronounceably higher than in the vicinity of the initial, zero deflection, configuration. While a possibility to operate the device in the proximity of the PI point is limited due to the danger of the stability loss and the PI collapse, the ST jump is reversible. However, the device may require reset after the stability loss event. In this context, configurations, corresponding

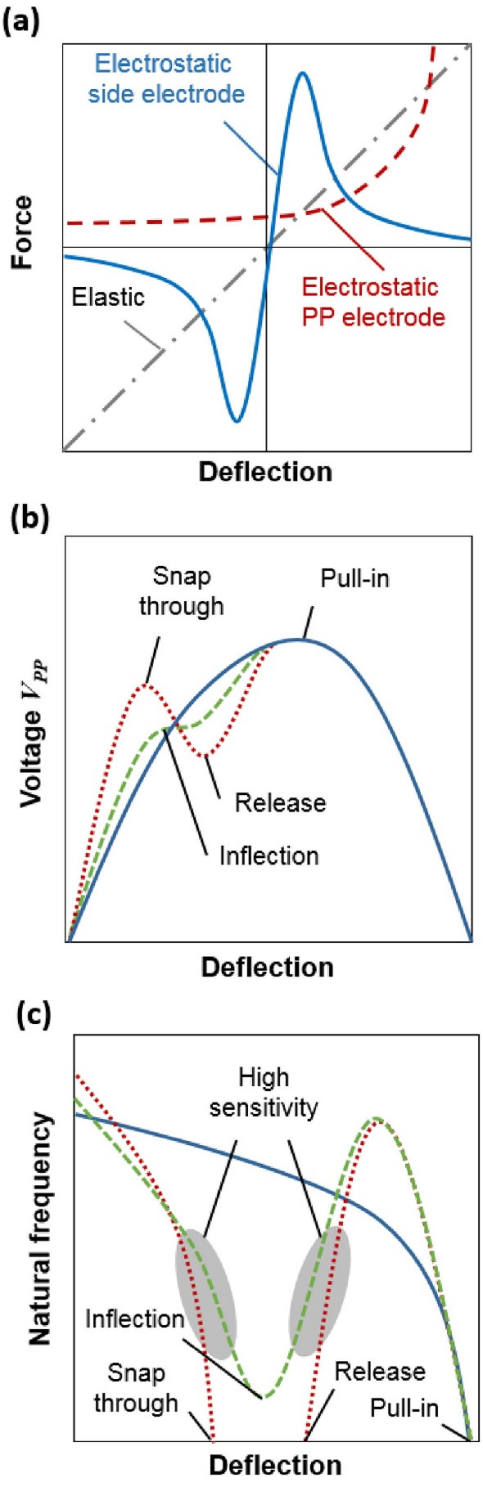

Figure 2. (a) Schematic representation of the forces acting on the beam: the fringing field (S electrode) restoring electrostatic force (blue), the electrostatic PP electrode divergent force (red) and the elastic mechanical restoring force (gray line) E. (b) Resulting equilibrium curve for $V_s = 0$ (solid line), close to the critical, bistability threshold value (dashed line) and for higher V_s leading to the bistable behavior (dots). (c) The natural frequency of the beam as a function of the beam's deflection $V_s = 0$ (solid line), for critical V_s (dashed line) and for V_s corresponding to the bistable behavior (dots). In the vicinity of the inflection point, high sensitivity is observed (gray-shaded regions).

to the bistability threshold (dashed lines in figures 2(b) and (c)), are promising since they allow smooth, continuous operation without compromising frequency sensitivity.

To provide a more quantitative description of the device behavior, we present a model of the beam attached to a vibrating substrate and simultaneously actuated by the PP and the S electrodes. The beam dynamics, considered in the framework of the Bernoulli–Euler theory, are governed by the equation

$$EI_{yy}\frac{\partial^4 w}{\partial x^4} + c\dot{w} + \rho A\ddot{w} = f_{pp} - f_s H(x - x_S) - \rho A a_B. \qquad (3)$$

Here A and I_{yy} are the respective area and the second moment of area of the beam cross section, c is the viscous damping coefficient and $a_B(t)$ is the time-dependent acceleration of the substrate. Hereafter, overdots $\dot{(\ )} = \partial/\partial t$ denote derivatives with respect to the spatial coordinate x and time t, respectively. The distributed electrostatic forces f_{PP} (equation (2)) and f_S (equation (1)) correspond to the PP and the S electrodes, respectively. The Heaviside step function $H(x)$ is introduced to take into account that the force f_S is applied only to the end part of the beam where $x > x_s = L—L_s$, figure 1. Our calculations show that the static deflection of the beam due to gravity is of the order of few tens of nm, which is much less than the beam thickness, and can therefore be neglected. In general, due to the interaction and capacitive coupling between the PP and the S electrodes, the resulting electrostatic force acting on the beam cannot be calculated just by simply superimposing the forces f_{PP}, equation (2) and f_S, equation (1) [32, 44]. However, to highlight the role of the interplay between the leading factors that influence the device response in the framework of the simplest possible model, we disregard the interaction and consider the contribution of each of these forces separately, as reflected by equation (3). Despite its approximate character and simplicity, the model provides important insights into the key features of the device behavior and contribution of each of the loading factors on the beam's response.

Using the single degree of freedom Galerkin approximation $w(x,t) \approx w_m(t)\phi(x)$, the reduced-order (RO) model of the beam is built. Equation (1) is reduced to the ordinary differential equation (see [40] for details)

$$\begin{aligned} &EI_{yy}I_1\, w_m + cI_2\dot{w}_m + \rho AI_2\ddot{w}_m \\ &\quad = \frac{\varepsilon b V_{pp}^{\,2}}{2}\int_0^{L_{pp}} \frac{\phi}{(g_{PP} - w_m\phi)^2}dx - \frac{a\sigma V_S^{\,2}(w_m/d)}{(1+\sigma|w_m/d|^p)}I_2^S \\ &\quad - \rho A a_B I_3 \end{aligned} \qquad (4)$$

where $w_m = w(L)$ is the beam's endpoint deflection, $\phi(x)$ is the fundamental Eigen mode of the cantilever and

$$I_1 = \int_0^L \left(\frac{d^2\phi}{dx^2}\right)^2 dx,\ I_2 = \int_0^L \phi^2 dx,\ I_2^S = \int_{x_S}^L \phi^2 dx,\ I_3 = \int_0^L \phi dx. \qquad (5)$$

The equilibrium endpoint deflection $w_m^* = w_m^*(V_{PP}, V_S)$ (hereafter stars $(\bullet)^*$ denote static equilibrium values) satisfies the static counterpart of equation (4), where all the time derivatives are set to zero

$$\left[EI_{yy}I_1 + \frac{\left(a\sigma {V_S}^2/d\right)}{\left(1+\sigma|w_m^*/d|^p\right)} I_2^S\right] w_m^* = \frac{\varepsilon b {V_{pp}}^2}{2}\int_0^{L_{pp}} \frac{\phi}{\left(g_{PP} - w_m^*\phi\right)^2}\mathrm{d}x. \tag{6}$$

In equation (6), the left-hand side represents the restoring (linear elastic and the nonlinear, provided by the S electrode) electrostatic forces while the right-hand side is associated with the diverging electrostatic force provided by the PP electrode.

To obtain the approximate expression for the frequency of the free undamped vibrations around the equilibrium, we substitute $w_m(t) = w_m^* + v(t)$, $c = 0$, $a_B = 0$ into equation (4). By linearizing the resulting expression around w_m^* and by taking into account equation (6) we obtain the effective mass $M_{\text{eff}} = \rho A I_2$ and the effective stiffness

$$K_{\text{eff}} = EI_{yy}I_1 + \frac{\left(a\sigma V_S^2/d\right)\left(1-\sigma(p-1)(w_m^*/d)^p\right)}{\left(1+\sigma|w_m^*/d|^p\right)^2} I_2^S - \frac{\varepsilon b V_{pp}^2}{2}\int_0^{L_{pp}} \frac{\phi^2}{\left(g_{PP} - w_m^*\phi\right)^3}\mathrm{d}x \tag{7}$$

of the beam. Consequently, the linearized frequency associated with equation (4) is

$$f_{\text{eff}} = f_0\Bigg(1 + \left(\frac{a\sigma I_2^S V_S^2}{EI_{yy}I_1 d}\right)\frac{1-\sigma(p-1)(w_m^*/d)^p}{\left(1+\sigma|w_m^*/d|^p\right)^2} - \frac{\varepsilon b V_{pp}^2}{2EI_{yy}I_1}\int_0^{L_{pp}} \frac{\phi^2}{\left(g_{PP} - w_m^*\phi\right)^3}\mathrm{d}x\Bigg)^{\frac{1}{2}}. \tag{8}$$

Here $f_0 = (1/2\pi)\sqrt{I_1 EI_{yy}/(I_2\rho A)} = \left(\lambda_1^2/2\pi\right)\sqrt{EI_{yy}/(\rho A L^4)}$ is the mechanical (corresponding to the unactuated state) frequency of the beam, where $\lambda_1 \approx 1.875$ is the fundamental eigenvalue of the cantilever. Equations (7) and (8) show that an increase in V_S results in the increase of the effective stiffness and of the associated natural frequency. In contrast, an increase in V_{PP} reduces the K_{eff} and results in the softening of the device. The nonlinearity associated with f_{PP} is of a softening type [42]. The nonlinearity associated with of f_S is also of a softening type, even for deflections smaller than the value corresponding to the inflection point on the deflection–electrostatic force curve, figure 2(a) [31].

3. Electrostatic force mapping

In order to obtain the fitting parameters appearing in the expression for f_S in equation (1), a two-dimensional finite element (FE) analysis of the electrostatic problem within a region surrounding the beam and the electrodes was carried out. The COMSOL Multiphysics package was used for this purpose. The dimensions of the beam are listed in table 1. The electrostatic computational domain was a square with the dimensions of 200 × 200 μm, figure 3(a). Zero potential boundary condition $V = 0$ was enforced on the outer surrounding boundary of the computational domain and on the boundary of the rectangular beam's cross-section with the dimensions $d \times b$. The potential of 1 V was enforced on the S electrode. The computational domain was meshed using 53 000 triangular elements. The electrostatic problem was solved multiple times for the electric potential, every time for a different position of the beam cross-section along the vertical z-axis, figure 3(a). For each position of the beam, the electrostatic force was calculated. Since the model is two-dimensional, the analysis provided the force per unit length of the cantilever. The FE results were least-square fitted using the Pade function (equation (1)) and the values of the fitting parameters were found to be $p = 2.44$, $\sigma = 0.27$, $\alpha = 2.3\ 10^{-6}$ N (V^{2}m). The distribution of the electric potential for one of the configurations is illustrated on figure 3(b).

Table 1. Parameters of the beam used in calculations.

Parameter	Value (μm)
L	2000
d	5
b	16
g_S	5
L_S	750
E	169

In order to estimate the role of the electrostatic coupling between the S and the PP electrodes, the electrostatic force was also calculated for the configuration containing both the S and the PP electrodes. The PP electrode of the width of 200 μm was located at the distance of $g_{PP} = 180$ μm from the beam. For these PP electrode parameters, the snap-through is possible, the associated deflections are comparable with the cantilever thickness and are far from the critical PI point. The electrostatic computational domain was extended to the size of 700 × 700 μm. The result, in terms of the electric potential, is shown in figure 3(c). Strong interaction between the S and the PP electrode is observed. A comparison between the uncoupled model, when the forces provided by the S and the PP electrodes are calculated separately and then superimposed, and the force obtained using the model containing both electrodes (figure 3(c)) is presented in figure 3(d). While the discrepancy between the two models is somehow significant (up to 30%), the approximate approach still captures qualitatively the leading features of the dependence between the force and the beam deflection. Specifically, the model predicts a force curve maximum and the character of the force decay. While general mapping of the force can be built in principle, the procedure requires fitting of the entire capacitance matrix for each position of the beam, which is computationally intensive [45]. In the present work, for the sake of simplicity

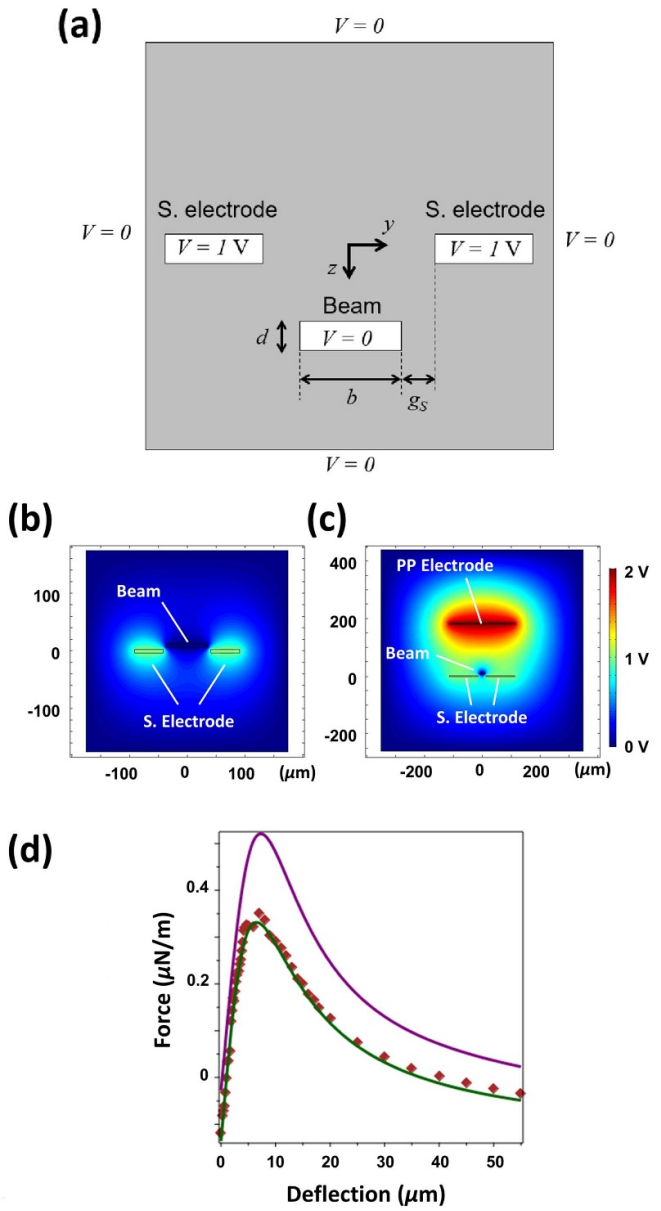

Figure 3. Numerical results for the electrostatic potential for (a) beam's cross-section by the *yz* plane (b) with the S electrodes ($V_S = 1$ V) only, and (c) with the S electrodes and the PP electrode ($V_S = 1$ V, $V_{PP} = 2$ V). In both (a), (b) the beam is located 10 μm away from the S electrode center. (d) The forces (per unit length) acting on the beam for Vs = 1 V and $V_{PP} = 2$ V. The purple curve shows the force calculated using the uncoupled approach, with the S electrode forces and the PP force evaluated separately using equations (1) and (2), respectively. Polynomial functional fit (green line) to the FEM results (dots) from the full electrostatic field analysis.

and transparency of the development, we continue to calculate separately the forces provided by the S and the PP electrodes, by using equations (1) and (2), respectively. The resulting electrostatic force acting on the beam is then obtained by adding the contribution of each of the electrodes. We found that, despite its limitations, the simplified model qualitatively explains the experimental results and provides insight into the device behavior.

4. Model results

Calculations were carried out for the beam with the nominal dimensions listed in table 1. The geometry of the device is compatible with the adopted deep reactive ion etching (DRIE)-based fabrication process on the one side and makes it possible the device operational principle illustration on the other side. For example, the minimal distance g_S between the beam and the side electrode was limited by the contact lithography resolution while the device thickness, the length of the beam and of the side electrode were chosen to allow the enhanced electrostatic tunability demonstration at reasonably low actuation voltages of several tens of V. The deflection of the beam and the frequency of the free vibrations around the equilibrium were calculated as the functions of the applied voltages V_s and V_{pp}. Figure 4(a) illustrates the equilibrium of the beam and can be viewed as an evolution of the curve $V_{PP} = V_{PP}(w_m^*)$ with increasing V_S. At $V_S = 0$, the equilibrium curve $V_{PP} = V_{PP}(w_m^*)$is typical for a device actuated by a PP electrode. Further increase of V_{PP} may result in the PI instability. Increase of V_s results in the emerging of the inflection point followed by the appearance of bistability. Bistable behavior is observed at $V_S = 40$ V. Figure 4(b) shows the corresponding linearized natural frequency of the beam. Despite that V_{PP} is not shown on figure 4(b), since the deflection $w_m^* = w_m^*(V_S, V_{PP})$ depends on the voltages, the points of the frequency surface are mapped from the equilibrium surface, figure 4(a). The implication is that for any point on figure 4(a) with the coordinates (w_m^*, V_S, V_{PP}) there is a corresponding point on figure 4(b) with the coordinates (w_m^*, V_S, f).

Figures 4(a) and (b) are instrumental for the illustration of the frequency tuning by using the appropriate combination of V_{pp} and V_s. Specifically, in accordance with figure 4(a), when $V_S = 0$, the increase of the beam's deflection is accompanied by the decrease of the curve slope $\partial V_{PP}/\partial w_m^*$. Since the slope is related to the beam's effective stiffness, the frequency of the device decreases as well. This is the well-known case of the electrostatic softening when the stiffness and the frequency are decreased as the device approaches the PI instability. The corresponding path is shown by the arrow 1 in figure 4. In contrast, since the side electrode force is restoring, the increase of V_S results in the stiffening of the beam and in the increase of cantilever's frequency [31, 40]. For example, the increase of the slope $\partial V_{PP}/\partial w_m^*$ accompanying the increase in V_S is observed along the path shown by arrow 2 in figure 4. Arrow 3 shows the influence of V_S and V_{PP}. Within a certain range of deflections, the increase of $V_S$may actually result in a softening, rather than hardening, behavior. Path 3 is shown for the case of a constant deflection, and not constant V_{PP}. In this case, the softening emerges since the beam approaches the ST limit point with increasing V_S. In the context of resonant sensors, the configurations with the maximal frequency-surface slope $\partial f/\partial w_m^*$ and the corresponding range of deflections are ideal operating regimes that provide highest frequency to deflection sensitivity.

The results presented in figure 4 are shown for the case when the beam deflection is due to the force controlled by the PP electrode. In this scenario, the device can be viewed as a

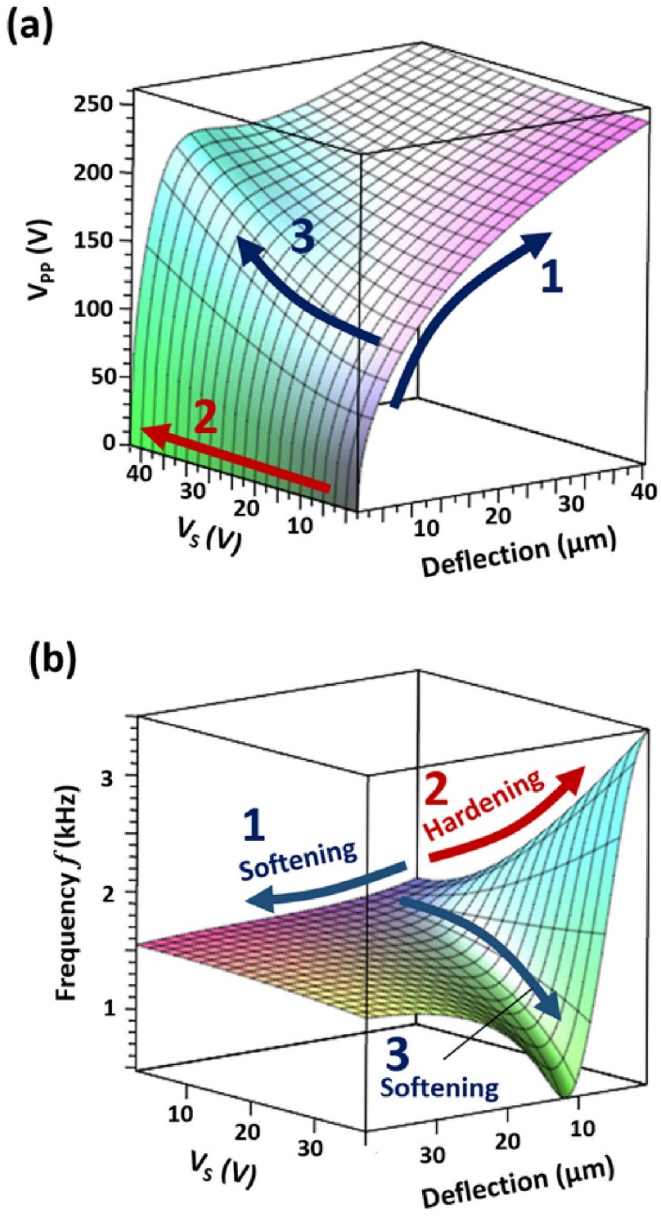

Figure 4. Model results. (a) The equilibrium surface. The emerging of the inflection point with increasing V_S is observed, followed by the appearance of the bistable behavior. (b) Natural frequency as a function of V_S and the deflection. The arrows marks numbered from 1 to 3, consistently in both (a) and (b), show possible tuning path: 1—softening due to the increased V_{PP} and V_S hold constant; 2—stiffening for increased V_S and zero deflection at $V_{PP} = 0$; 3—softening due to the increased V_S and nonzero deflection at $V_{PP} \neq 0$.

voltage sensor. Another interesting possibility is the case when PP electrode is movable and the PP force is parameterized by the distance g_{PP}between the beam and the PP electrode rather than by the voltage [16, 22]. In this framework, the voltages $V_{PP}$and V_S are kept constant. The resulting PP electrostatic force and consequently the frequency are affected by the PP electrode displacement. The region of maximal sensitivity with electrode displacement represents an ideal operating regime for resonant displacement sensing applications [22].

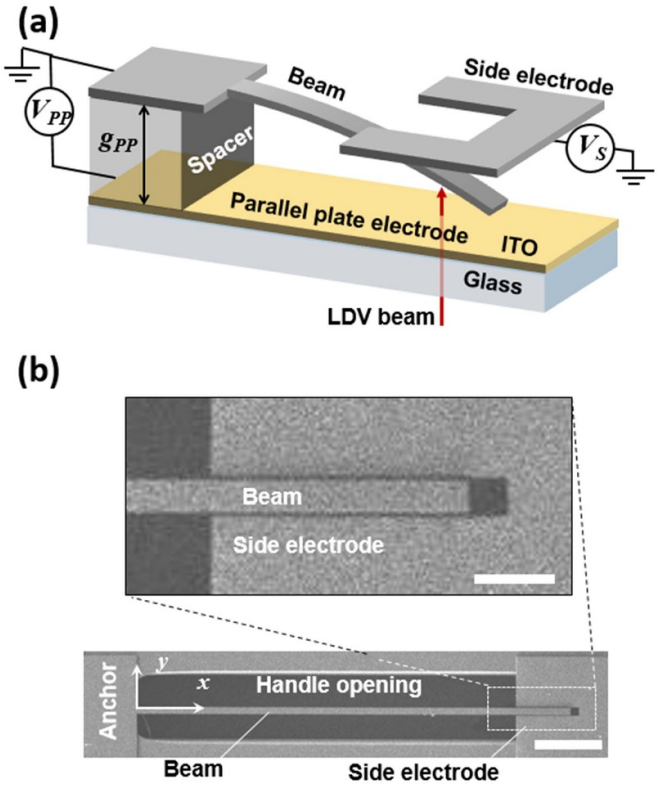

Figure 5. (a) Schematic view of the integrated device used in the first experiment. The beam and the S electrode were attached via a polymeric spacer to commercial ITO on glass, serving as the PP electrode. Transparency allows optical interrogation of the beam dynamics using laser doppler vibrometry (LDV) through the PP electrode. (b) Scanning electron micrographs of the fabricated devices. Scale bar is ≈300 μm. The PP ITO electrode is not shown. Scale bar for the zoomed-in micrograph is ≈100 μm.

5. Experiments

Using DRIE, cantilevers and electrodes were fabricated from a $d \approx 5$ μm thick single crystal silicon device layer of a SOI wafer with $a \approx 2$ μm thick buried thermal silicon dioxide layer. DRIE was also used to etch a cavity within the handle wafer. The cavity was necessary to allow large unobscured vibrations of the beam and to prevent stiction. The devices were released using a vapor-based hydrofluoric acid process.

Two types of experiments were conducted. The goal of the first experiment was to explore the influence of V_{PP} and V_S on the cantilever frequency and to demonstrate the wide range frequency tuning. In this experiment, we used a glass slide with deposited transparent conductor, Indium Tin Oxide (ITO), as the PP electrode. The transparent electrode-substrate combination allowed for optical interrogation of the beam. Using an insulating polymer spacer, cut out of a commercially available sheet with a thickness of $g_{PP} \approx 180$ μm, the device was attached to the slide in such a way that the device layer of the SOI die faced the ITO layer. Figure 5 shows a scanning electron micrograph of the fabricated device with the dimensions $L \approx 2000$ μm, $b \approx 16$ μm, $d \approx 5$ μm, $g_S \approx 5$ μm and $L_S \approx 750$ μm. The experimental setup is illustrated in figure 6. The chip was mounted onto a custom-built PCB. The beam and

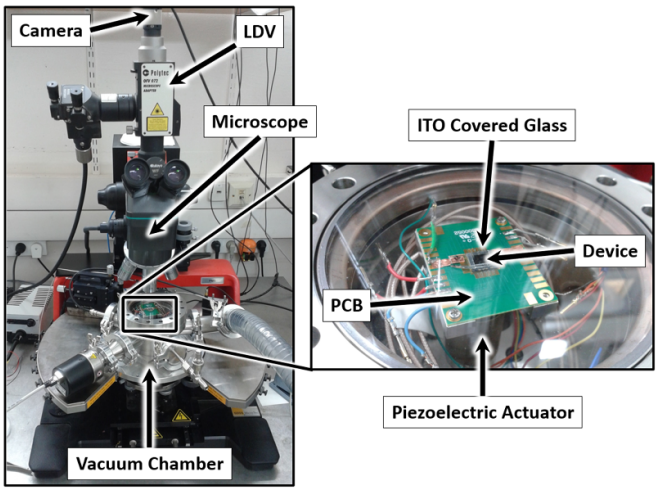

Figure 6. Experimental setup consists of a vacuum chamber positioned on the wafer prober under a microscope with a LDV. The device is mounted onto a printed circuit board (PCB) board, which is attached to an external piezoelectric lead zirconium titanate (PZT) actuator (shaker). ITO on the glass coverslip is attached with conductive tape.

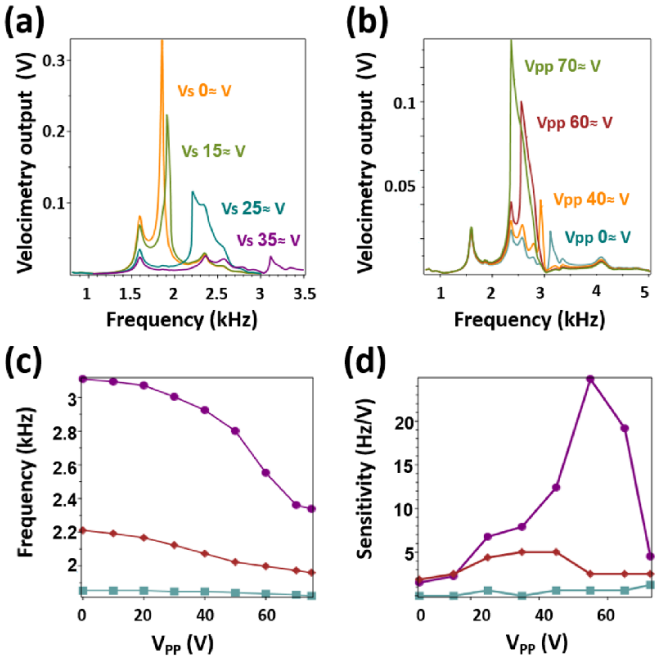

Figure 7. Results of the first experiment demonstrating the wide range frequency tuning. (a) Measured frequency spectra of the beam for $V_{PP} = 0$ and different values of V_s, demonstrating electrostatic stiffening effect. (b) Measured frequency spectra, using a ≈10 V AC actuation signal, of the beam for $V_S \approx 35$ V at different values of V_{PP}. In both (a), (b) the horizontal axis represents the piezoelectric actuator frequency. (c) Resonant frequencies of the beam, actuated by the PP and the S electrodes, as functions of the PP electrode voltage V_{PP}, for $V_S \approx 0$ (square), $V_S \approx 25$ V (diamond) and $V_S \approx 35$ V (circle). (d) Frequency sensitivity to the PP electrode voltage.

the side electrode were wire bonded to the PCB contact pads. The PCB, in turn, was attached to an external piezoelectric actuator. The assembly containing the chip-PCB-piezoelectric actuator stack was covered by the ITO slide, then placed into a custom-built vacuum chamber and pumped down to pressure of ≈480 Pa. The chamber was placed onto a wafer prober under an optical microscope. Using a network analyzer, a sinusoidal, zero offset, voltage signal of ≈10 V was applied to the piezoelectric actuator. For the out-of-plane, inertial excitation of the beam, the applied frequency was swept varied between ≈1 and ≈5 kHz. In addition, steady-state voltages V_{PP} and V_S were supplied by separate voltage sources to the parallel plate and to the side electrodes, respectively. We used a single-beam LDV in a velocity acquisition mode to measure the out-of-plane response of the beam. The output of the LDV was fed back into the network analyzer. In parallel to the spectral analysis of the output signal, the velocity time history provided by the LDV was measured in real time with an oscilloscope.

The resonant curves are shown in figure 7(a). In the case when $V_S = V_{PP} = 0$, the measured resonant frequency of the beam was ≈1.85 kHz. The calculated natural frequency of the beam, using nominal dimensions, is ≈1.73 kHz. We attribute the slight discrepancy to the uncertainty in the beam's geometry. The experiment was repeated for several values of V_s. Increasing V_S from zero to $V_S \approx 35$ V caused a frequency change of ≈67%, from ≈1.85 to ≈3.1 kHz, demonstrating, consistently with the qualitative model prediction, (equation (7) and figure 4(b), arrow 2) the significant electrostatic stiffening effect. The stiffening of ≈67% reported here is higher than the previously reported values (≈11% in [31], ≈20% in [34]) and is achieved at significantly lower actuation voltages. In accord with [31, 41, 42] for all V_S values lateral (in the y-direction) PI instability was not observed during our experiments. This observation can be attributed to the fact that during the operation the deflection of the device statically (by pp voltage) and dynamically actuated in the vertical z direction was comparable or higher than the beam's thickness. As a result, the electrostatic force in the lateral y-direction was much smaller than the full static value associated with the initial configuration, which also may reduce the danger of the side PI. The electrostatic softening due to the PP electrostatic force is shown in figure 7(b). The results suggest that the response is nonlinear and indicative of a softening nonlinearity [46] associated with the configuration-dependent actuating electrostatic forces, equation (4). Since the system demonstrates softening nonlinearity and the excitation frequency is swept up, the peak values of the resonant curves on figure 7(b) are associated with the jump in the resonant response [46] and do not represent the (effective) linear resonant frequencies of the beam. To illustrate the electrostatic softening, which manifests itself in the frequency decrease with increasing V_{PP}, because this is not a linear Lorentzian peak, we used the frequency peak value for comparison. Figure 7(b) shows a decrease in the peak value (jump) frequency with increasing V_{PP}. As expected, since the frequency decrease is related to a decrease of the effective stiffness of the beam, larger amplitudes are measured for higher values of V_{PP}. Figure 7(c) shows measured peak frequency as a function of V_{PP}, each curve corresponding to a distinct value of V_S. In all the cases, as predicted by equation (7), the frequency decreases with increasing V_{PP} with

the decrease being more pronounced for higher V_S. The sensitivity of the cantilever to V_{PP} is represented by the slope of the curves in figure 7(b). Our data show that for the small amplitude vibrations at $V_S = 0$, the cantilever's frequency is only slightly affected by the electrostatic loading provided by the PP electrode. In contrast, at $V_S \approx 35$ V, the frequency change of ≈25% is observed, from ≈3.1 to ≈2.35 kHz. In terms of the frequency to loading sensitivity (figure 7(d)), our results demonstrate a 20-fold enhancement of the sensitivity. These experiments, with the use of the static (rigid) ITO PP electrode, show all the leading frequency tuning effects as qualitatively predicted by the model. Our data show stiffening due to increasing V_S, softening when additional V_{PP} is applied, and the frequency to V_{PP} (frequency to loading) sensitivity enhancement achieved by increasing V_S.

The goal of the second set of experiments was (a) to demonstrate feasibility of a spectral-based deflection sensing approach and (b) to show the frequency to deflection sensitivity enhancement using fringing electrostatic field actuation. These scenarios require a movable electrode. In our experiments we used a pressurized flexible plate ('membrane') as a movable electrode. Using a SOI wafer, circular ≈5 μm thick Si membranes, ≈2000 μm in diameter were fabricated from the device layer. This was achieved by DRIE circular cavities in the SOI wafer handle with the buried oxide layer serving as an etch stop. The remaining silicon dioxide layer was then etched using a vapor-based hydrofluoric acid process. Following device fabrication, the geometry of the device was measured by laser confocal microscopy. Due to the residual stress and stress gradients in the multilayer assembly containing two SOI wafers, incorporating several Si and SiO_2 layers and polymeric spacers, the released cantilevers and the side electrodes were not fully coplanar. We measured a deflection of ≈7 μm at the free-end of the beams.

To attach the cantilever die to the membrane in such a way that the device layer is facing the membrane, polymer spacer of the thickness $g_{PP} \approx 220$ μm was used (figure 8). The assembly, containing the cantilever and the membrane dies, was mounted onto a custom-built PCB. The beam and the side electrode were wire-bonded to the PCB contact pads. The double chip and the PCB stack assembly were placed onto a wafer prober so that the membrane was positioned above the sink hole. The sink hole was directly connected to a vacuum pump that provided a variation in chamber pressure between $P \approx 5$ kPa and up to $P \approx 70$ kPa. The pressure was set manually using an external pressure gage and was measured with the accuracy of ≈1 kPa. The side of the membrane facing the cantilever was at the ambient atmospheric pressure. The velocity response of the cantilever was measured using the LDV through the openings in the handle of the SOI wafer and in the PCB. The position of the laser spot of the LDV was monitored, through the wafer handle cavity, using the wafer prober microscope. The voltage signals supplied to the cantilever were supplied by the network analyzer, which was also used to acquire the output of the LDV.

The sinusoidal, zero offset, voltage signal with an amplitude of $V_{AC} \approx 1$ V was applied to the cantilever. The frequency was swept between ≈1 and ≈2 kHz. In addition,

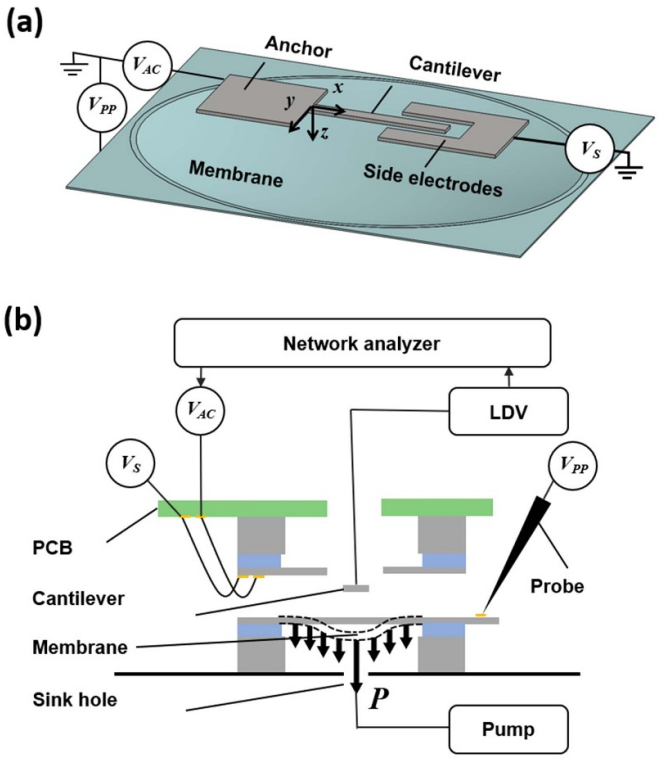

Figure 8. (a) Schematic illustration of the movable-electrode experimental setup. (a) The cantilever is positioned in the proximity of a deformable pressurized membrane that serves as a movable electrode. Handle layers of the SOI wafers are not shown. (b) The device stack containing two SOI dies attached to a PCB board. The PCB-die assembly is placed onto the wafer prober chuck in such a way that the membrane is positioned above the sink hole. Cantilever vibrations were measured by the LDV through openings in the wafer handle and in the PCB.

using a separate power supply, time-independent, steady-state voltages V_{PP} and V_S were applied to the membrane and the S electrode, respectively. The experiments were carried out under various combinations of V_S and V_{PP}. Figure 9(a) shows the resonant curves of the beam for increasing V_S with $V_{PP} = 0$. An increase of $V_S = 0$ to $V_S \approx 18$ V, resulted in a decrease of the resonant frequency from ≈1720 to ≈1605 Hz, respectively. This corresponds to the relative frequency shift of $|f_{eff} - f_0|/f_0 \times 100 \approx 6.6\%$. While stiffening effect due to fringing electrostatic fields was previously reported by many authors [20, 31, 37], softening associated with the fringing fields was rarely addressed [34]. A repelling cantilever actuator operated by fringing fields demonstrated softening of ≈20% (in terms of the relative frequency shift) [34] when actuated by the voltages of 200 V, which are much higher than used in the present work. The softening registered in the second experiment stands in a contradiction to the results of the first experiment, which showed the hardening with increasing V_S, figure 7(a). We attribute the softening effect in the second experiment to the initial deflection of the beam in the unforced, as fabricated, configuration. In accordance with figure 4(b), due to even a small initial deflection, the hardening can be replaced by softening accompanying an increase of the side electrode voltage.

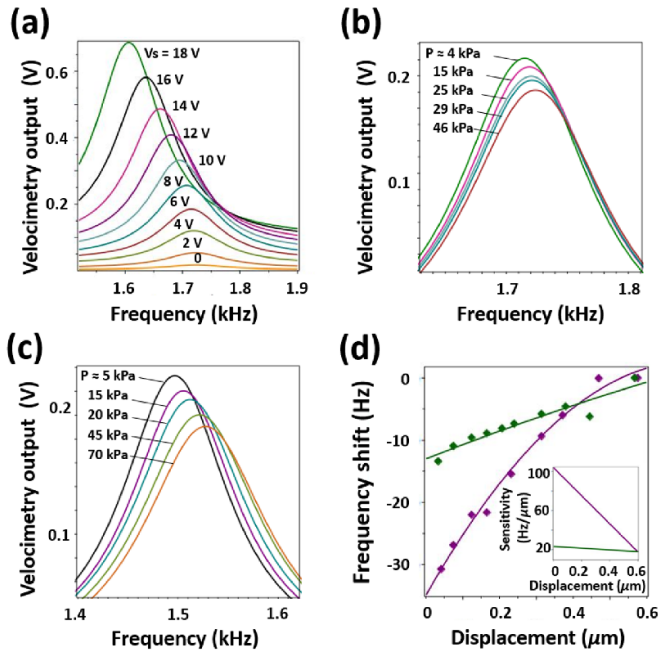

Figure 9. Experimental results of the second experiment, demonstrating the deflection sensing approach and the frequency to deflection sensitivity enhancement using fringing electrostatic field actuation. (a) Measured frequency spectra of the beam for $V_{PP} =$ and for different values of V_S, from $V_S \approx 0$ V up to $V_S \approx 18$ V demonstrating electrostatic softening. Measured frequency spectra of the beam, for the case of (b) $V_S \approx 0$ V and (c) $V_S \approx 25$ V, with $V_{PP} \approx 45$ V, and for different displacements of the membrane (the parallel plate electrode) varying between $\approx$0.03 μm and $\approx$0.56 μm. (d) Frequency shift as function of membrane displacement, for $V_S \approx 0$ V (green) and $V_S \approx 25$ V (purple). The solid lines are polynomial fits of the measured results. Inset shows the sensitivity of the frequency to the PP electrode displacements.

Next, the influence of the PP electrode displacements and of the S electrode voltage on the frequency was investigated. The deflection of the membrane was controlled by varying the pressure. In order to estimate the measured frequency sensitivity to the PP electrode displacement, the pressure was applied to the membrane. For a given pressure P, the midpoint deflection w_0 can be calculated as the solution of the following cubic algebraic equation [47]

$$w_0 = \frac{3PD^4(1-\nu^2)}{256Ed^3\left(1+\frac{0.488w_0^2}{d^2}\right)}. \tag{9}$$

Here, ν is the Poisson's ratio of the membrane material and D is the membrane diameter. The implicit form of equation (9) emphasizes that membrane deflection is strongly affected by the geometric nonlinearity due to membrane constrained in-plane tension. The measured frequency spectra of the cantilever with $V_{PP} \approx 45$ V and membrane displacements varying between $w_0 \approx 0.03$ μm and up to $w_0 \approx 0.56$ μm, for $V_S \approx 0$ V and $V_S \approx 25$ V are shown in figures 9(b) and (c), respectively.

Figure 9(d) shows the resonant frequency shift as a function of the membrane displacement, for $V_S \approx 0$ V and $V_S \approx 25$ V. The frequency of the cantilever increases when the pressure, and therefore the deflection of the membrane, increases. During stiffening, as the membrane deflects the gap increases between the PP electrode and the beam and in turn the PP electrostatic force acting on the beam decreases. Consequently, this gives rise to two scenarios. The first is that the smaller PP force implies a less pronounced softening, and, therefore, higher frequency (see figures 3(a) and 7(c)). Since this softening is related to the PP electrode force, softening is expected for both zero and non-zero values of V_S. The second consequence is that for a smaller PP force the deflection of the beam decreases, making the stiffening effect associated with the S electrode force to be larger. This is because the slope of the deflection—f_S curve is the largest at zero deflection, as shown in figures 2(a) and 4. The magnitude of the frequency shift is strongly affected by the value of the side-electrode voltage V_S. For example, a shift of $\approx$30 Hz was measured for $V_S \approx 25$ V, while only 13 Hz shift was measured at $V_S = 0$. Inset in figure 9(d) shows the frequency sensitivity $\partial f/\partial w_m^*$ as calculated from the slope of the curve fitting the measured data. For $V_S = 0$, the measured sensitivity was $\approx$23 Hz μm^{-1}. In contrast, when the applied S electrode voltage was increased to $V_S \approx 25$ V, the sensitivity increased to $\approx$98 Hz μm^{-1}, showing more than a fourfold increase in the scale factor of the sensor.

6. Conclusion

In this work, an approach for sensitivity enhancement of resonant cantilever-type displacement sensors is introduced and investigated both theoretically and experimentally. To improve the sensitivity of the device's effective stiffness and frequency to the parameters of interest, we introduced an additional nonlinearity by actuating the beam using fringing electrostatic fields. The dependence between the beam's frequency and the measured parameters, such as the actuation voltages, or, alternatively, the electrode's displacement, was tailored by varying the electrodes design and choice of the operating voltages.

The RO model of a cantilever actuated by a gap-closing, parallel plate electrode and by a side, coplanar with the beam electrode, was built using the Galerkin approximation. The parallel plate electrode provided a distributed transversal loading resulting in the bending of the beam in the direction apart from its initial, as fabricated, configuration. The side electrode is the source of the fringing electrostatic field resulting in a restoring electrostatic force controlled by voltage. The actuating force associated with the complex fringing fields was calculated by solving the electrostatic problem numerically, by means of the FE method.

Using the model, the maps were built presenting the relations between the PP and the S electrode voltages, the cantilever deflection and the linearized natural frequency, defined as the frequency of free undamped vibrations around an equilibrium point. Our model results show that the frequency of the beam can be tuned by using the actuating voltages. Moreover, the characteristic response can be switched from softening, when the frequency decreases with the increasing actuating

voltages or deflection, to stiffening, which manifests itself in the increase of the frequency with increasing actuation voltages. One of the distinguishing features of the suggested geometry is that the cantilever actuated by a transverse PP electrode loading and by the S electrode, is bistable. When the device configuration is close to the bistability threshold, very small changes in the parameters, such as the actuating voltage, beam deflection or the distance between the beam and the electrode, leads to a significant shift in the frequency and even in the change in the response from softening to stiffening. This high tunability is an intrinsic beneficial feature of the suggested architecture and is the main source of the enhanced sensitivity of the device.

Two types of experiments were carried out using devices fabricated from single crystal Si by DRIE. In the first experiment, the beam was actuated by the unmovable PP and S electrodes. We studied dependence between the beam's frequency and each of the voltages applied to the electrodes. In agreement with the model prediction, we showed that the application of the voltage V_S to the S electrode results in the stiffening of the beam, while the increase of the PP electrode voltage V_{PP} is accompanied by softening. Specifically, frequency up tunability of ≈67% (at $V_S \approx 35$ V) and frequency decrease of ≈25% (at $V_{PP} \approx 70$ V and $V_S \approx 35$ V) were demonstrated. More importantly, the application of $V_S \approx 35$ V, in addition to V_{PP}, leads to ×20 increase of the beam's frequency sensitivity to the PP electrode voltage. In the second experiment, the cantilever frequency sensitivity to the deflection of a flexible pressurized membrane serving as a movable electrode was studied. Our experiments show that increase of the S electrode voltage from $V_S \approx 0$ to $V_S \approx 25$ V increases the device sensitivity by more than ×4, from ≈23 to ≈98 Hz μm^{-1}.

The two scenarios of the electrode displacement sensing showed in the second experiment—with and without S electrode voltage—can be considered as two approaches for frequency-based displacement sensing. The case of zero V_s illustrates the cantilever frequency monitoring approach, which is widely used, yet, is still less common compared to capacitance or piezoresistive sensing. In order to compare these results to the common capacitive sensing approach, both input (deflection) and output (frequency) values were normalized by calculating the relative change of the frequency per relative change of the gap, i.e. $(\Delta f/f_0)/(\Delta w/g_0)$. In the case of the quasi-static capacitive sensing, the relative change of the capacitance (the gain) is $(\Delta C/C_0)/(\Delta w/g_0) = 1$. Based on our experimental results, a relative frequency shift of $(\Delta f/f_0)/(\Delta w/g_0) \approx 3$ was obtained for $V_S = 0$. Therefore, the cantilever frequency monitoring approach, even without fringing field related enhancement, is more sensitive than direct capacitive sensing. Our experimental results show that in the case with $V_S \approx 25$ V applied to the S electrode, the relative frequency shift reached the value of $(\Delta f/f_0)/(\Delta w/g_0) \approx 14$. The ratio between the relative sensitivities corresponding to $V_S \approx 25$ V and $V_S = 0$ is $14/3 = 4.6$.

The approach considered in the present work can be implemented for the performance enhancement of a large variety of sensors. For example, in the inertial sensors such as accelerometers and gyroscopes, cantilever frequency monitoring will allow measurements of the proof mass deflections with higher sensitivity and lower $1/f$ noise. The same approach can be beneficial also in AFM, acoustic, mass, and biochemical sensors. Since the main goal of the present work was to explore the feasibility of the suggested concept, the parameters of the devices explored were not optimized. We can argue that more careful design and optimization of the device architecture and operational parameters, as well as downscaling of the cantilever dimensions to the nanoscale, may allow further improvements in the sensor performance.

Data availability statement

The data that support the findings of this study are available upon reasonable request from the authors.

Acknowledgments

The devices were fabricated and tested at the Center for Nanoscale Science & Technology (CNST) at the National Institute of Standards and Technology (NIST) and at the Microsystems Design and Characterization Laboratory at Tel Aviv University. The work of Slava Krylov was supported by the Henry and Dinah Krongold Chair of Microelectronics. Certain commercial equipment, instruments, or materials are identified in this paper in order to specify the experimental procedure adequately. Such identification is not intended to imply recommendation or endorsement by NIST, nor is it intended to imply that the materials or equipment identified are necessarily the best available for the purpose.

ORCID iDs

Naftaly Krakover https://orcid.org/0000-0002-1009-7147
Slava Krylov https://orcid.org/0000-0003-3759-6808

References

[1] Alvarez M and Lechuga L M 2010 Microcantilever-based platforms as biosensing tools *Analyst* **135** 827
[2] Boisen A, Dohn S, Keller S S, Schmid S and Tenje M 2011 Cantilever-like micromechanical sensors *Rep. Prog. Phys.* **74** 36101
[3] Li M, Tang H X and Roukes M L 2007 Ultra-sensitive NEMS-based cantilevers for sensing, scanned probe and very high-frequency applications *Nat. Nanotechnol.* **2** 114–20
[4] Shekhawat G, Tark S-H and Dravid V P 2006 MOSFET-embedded microcantilevers for measuring deflection in biomolecular sensors *Science* **311** 1592–5
[5] Morita S, Giessibl F J, Meyer E and Wiesendanger R 2015 *Noncontact Atomic Force Microscopy* vol 3 (Berlin: Springer)
[6] Rhoads J F, Shaw S W and Turner K L 2010 Nonlinear dynamics and its applications in micro- and nanoresonators *J. Dyn. Syst. Meas. Control* **132** 034001
[7] Younis M I 2011 *MEMS Linear and Nonlinear Statics and Dynamics* vol **20** (London: Springer Science & Business Media)

[8] Chivukula V B and Rhoads J F 2010 MEMS bandpass filters based on cyclic coupling architectures *Proc. of the ASME Int. Design Engineering Technical Conf. and Computers and Information in Engineering Conf. 2009, DETC2009* vol 6 pp 623–34

[9] Zhang W-M, Yan H, Peng Z-K and Meng G 2014 Electrostatic pull-in instability in MEMS/NEMS: a review *Sens. Actuators* A **214** 187–218

[10] Chowdhury S, Ahmadi M and Miller W C 2005 A closed-form model for the pull-in voltage of electrostatically actuated cantilever beams *J. Micromech. Microeng.* **15** 756–63

[11] Ramini A, Younis M I and Su Q T 2013 A low-g electrostatically actuated resonant switch *Smart Mater. Struct.* **22** 025006

[12] Benjamin E, Lulinsky S and Krylov S 2018 Design and implementation of a bistable force/acceleration sensing device considering fabrication tolerances *J. Microelectromech. Syst.* **27** 854–65

[13] Maiwald V *et al* 2018 Experimental fractal-like instability bands in a resonant silicon-silicon contact pull-in vibration detector *2018 IEEE Micro Electro Mechanical Systems (MEMS)* pp 984–7

[14] Khater M E *et al* 2014 Binary MEMS gas sensors *J. Micromech. Microeng.* **24** 065007

[15] Younis M I, Alsaleem F M, Miles R and Su Q 2007 Characterization of the performance of capacitive switches activated by mechanical shock *J. Micromech. Microeng.* **17** 1360–70

[16] Comi C, Corigliano A, Ghisi A and Zerbini S 2013 A resonant micro accelerometer based on electrostatic stiffness variation *Meccanica* **48** 1893–900

[17] Su J, Yang H, Fay P, Porod W and Bernstein G H 2009 A surface micromachined offset-drive method to extend the electrostatic travel range *J. Micromech. Microeng.* **20** 125–35

[18] Lee K B 2007 Non-contact electrostatic microactuator using slit structures: theory and a preliminary test *J. Micromech. Microeng.* **17** 2186–96

[19] Small J, Irshad W, Fruehling A, Garg A, Liu X and Peroulis D 2012 Electrostatic fringing-field actuation for pull-in free RF-MEMS analogue tunable resonators *J. Micromech. Microeng.* **22** 95004–10

[20] Ouakad H M 2014 Static response and natural frequencies of microbeams actuated by out-of-plane electrostatic fringing-fields *Int. J. Non-Linear Mech.* **63** 39–48

[21] Torun H, Sarangapani K K and Degertekin F L 2007 Spring constant tuning of active atomic force microscope probes using electrostatic spring softening effect *Appl. Phys. Lett.* **91** 253113

[22] Krakover N, Ilic B R and Krylov S 2016 Displacement sensing based on resonant frequency monitoring of electrostatically actuated curved micro beams *J. Micromech. Microeng.* **26** 115006

[23] Krylov S, Ilic B R and Lulinsky S 2011 Bistability of curved microbeams actuated by fringing electrostatic fields *Nonlinear Dyn.* **66** 403–26

[24] Su J, Yang H, Fay P, Porod W and Bernstein G H 2010 A surface micromachined offset-drive method to extend the electrostatic travel range *J. Micromech. Microeng.* **20** 015004

[25] Sulfridge M, Saif T, Miller N and O'Hara K 2002 Optical actuation of a bistable MEMS *J. Microelectromech. Syst.* **11** 574–83

[26] Medina L, Gilat R, Ilic B and Krylov S 2014 Experimental investigation of the snap-through buckling of electrostatically actuated initially curved pre-stressed micro beams *Sens. Actuators* A **220** 323–32

[27] Du X, Wang L, Li A, Wang L and Sun D 2017 High accuracy resonant pressure sensor with balanced-mass DETF resonator and twinborn diaphragms *J. Microelectromech. Syst.* **26** 235–45

[28] He S, Mrad R and Chong J 2011 Repulsive-force out-of-plane large stroke translation micro electrostatic actuator *J. Micromech. Microeng.* **21** 075002

[29] Batra R C, Porfiri M and Spinello D 2006 Capacitance estimate for electrostatically actuated narrow microbeams *Micro Nano Lett.* **1** 71

[30] Unterreithmeier Q P, Weig E M and Kotthaus J P 2009 Universal transduction scheme for nanomechanical systems based on dielectric forces *Nature* **458** 1001–4

[31] Linzon Y, Ilic B, Lulinsky S and Krylov S 2013 Efficient parametric excitation of silicon-on-insulator microcantilever beams by fringing electrostatic fields *J. Appl. Phys.* **113** 163508

[32] Kambali P N and Pandey A K 2017 Nonlinear coupling of transverse modes of a fixed–fixed microbeam under direct and parametric excitation *Nonlinear Dyn.* **87** 1271–94

[33] Pallay M and Towfighian S 2018 A parametric electrostatic resonator using repulsive force *Sens. Actuators* A **277** 134–41

[34] Pallay M, Daeichin M and Towfighian S 2017 Dynamic behavior of an electrostatic MEMS resonator with repulsive actuation *Nonlinear Dyn.* **89** 1525–38

[35] Suzuki Y, Miki D, Edamoto M and Honzumi M 2010 A MEMS electret generator with electrostatic levitation for vibration-driven energy-harvesting applications *J. Micromech. Microeng.* **20** 104002

[36] Pallay M and Towfighian S 2018 A reliable MEMS switch using electrostatic levitation *Appl. Phys. Lett.* **113** 213102

[37] Ozdogan M, Daeichin M, Ramini A and Towfighian S 2017 Parametric resonance of a repulsive force MEMS electrostatic mirror *Sens. Actuators* A **265** 20–31

[38] Hu F, Tang Y and Qian Y 2012 Design of a MEMS micromirror actuated by electrostatic repulsive force *Optik* **123** 387–90

[39] Ozdogan M, Towfighian S and Miles R 2017 A MEMS microphone with repulsive sensing *J. Acoust. Soc. Am.* **141** 3793

[40] Krakover N and Krylov S 2017 Bistable cantilevers actuated by fringing electrostatic fields *J. Vib. Acoust.* **139** 040908

[41] Krakover N, Ilic R and Krylov S 2018 Resonant pressure sensing using a micromechanical cantilever actuated by fringing electrostatic fields *2018 IEEE Micro Electro Mechanical Systems (MEMS)* pp 846–9

[42] Halevy O, Benjamin E B, Kessler Y and Krylov S 2021 Resonant sensing element realized as a single crystal Si cantilever actuated by fringing electrostatic fields *IEEE Sens. J.* **21** 10454–64

[43] Kaajakari V 2009 *Practical MEMS: Design of Microsystems, Accelerometers, Gyroscopes, RF MEMS, Optical MEMS, and Microfluidic Systems* (Las Vegas, NV: Small Gear Publishing)

[44] Kambali P N and Pandey A K 2016 Capacitance and force computation due to direct and fringing effects in MEMS/NEMS arrays *IEEE Sens. J.* **16** 375–82

[45] Pallay M, Miles R N and Towfighian S 2019 Merging parallel-plate and levitation actuators to enable linearity and tunability in electrostatic MEMS *J. Appl. Phys.* **126** 014501

[46] Nayfeh A H and Mook D T 1995 *Nonlinear Oscillations* (New York: Wiley)

[47] Timoshenko S P and Woinowsky-Krieger S 1959 *Theory of Plates and Shells* (New York: McGraw-hill)